J. Fluid Mech. (1997), *vol.* 353, *pp.* 285–312. Printed in the United Kingdom

© 1997 Cambridge University Press

Stokes flow in collapsible tubes: computation and experiment

By MATTHIAS HEIL†

Fluid Mechanics Laboratory, Massachusetts Institute of Technology, Cambridge, MA 02139, USA

(Received 14 January 1997 and in revised form 27 August 1997)

This paper is concerned with the problem of viscous flow in an elastic tube. Elastic tubes collapse (buckle non-axisymmetrically) when the transmural pressure (internal minus external pressure) falls below a critical value. The tube's large deformation during the buckling leads to a strong interaction between the fluid and solid mechanics.

In this study, the steady three-dimensional Stokes equations are used to analyse the slow viscous flow in such a tube whose deformation is described by geometrically nonlinear shell theory. Finite element methods are used to solve the large-displacement fluid–structure interaction problem. Typical wall deformations and flow fields in the strongly collapsed tube are shown. Extensive parameter studies illustrate the tube's flow characteristics (e.g. volume flux as a function of the applied pressure drop through the tube) for boundary conditions corresponding to the four fundamental experimental setups. It is shown that lubrication theory provides an excellent approximation of the fluid traction while being computationally much less expensive than the solution of the full Stokes equations. Finally, the computational predictions for the flow characteristics and the wall deformation are compared to the results obtained from an experiment.

1. Introduction

Many fluid conveying vessels in the human body are elastic and deform substantially in response to the traction exerted on them by the flow. Vessels which are subject to a positive transmural (internal minus external) pressure are inflated and retain their approximately cylindrical shape throughout the deformation. Since the vessel walls typically have a high extensional stiffness, such deformations tend to be of small amplitude.

However, numerous fluid conveying vessels are subject to a negative (compressive) transmural pressure and they collapse (i.e. buckle non-axisymmetrically) when the transmural pressure falls below a critical value. Examples of such vessels are the veins above the level of the heart, the airways during forced expiration, the pulmonary capillaries and the blood vessels in the heart muscle during systole. The buckling greatly reduces the vessel's structural stiffness. Therefore the wall deformations tend to be large and the collapse leads to a strong interaction between the wall deformation and the fluid mechanics. This strong fluid–structure interaction is responsible for phenomena such as the flow limitation observed during forced expiration and the development of large-amplitude self-excited oscillations, physiological examples of which include wheezing and the Korotkoff sounds heard during sphygmomanometry.

† Present address: Department of Applied Mathematics and Theoretical Physics, University of Cambridge, Silver Street, Cambridge CB3 9EW, UK.

https://doi.org/10.1017/S0022112097007490 Published online by Cambridge University Press

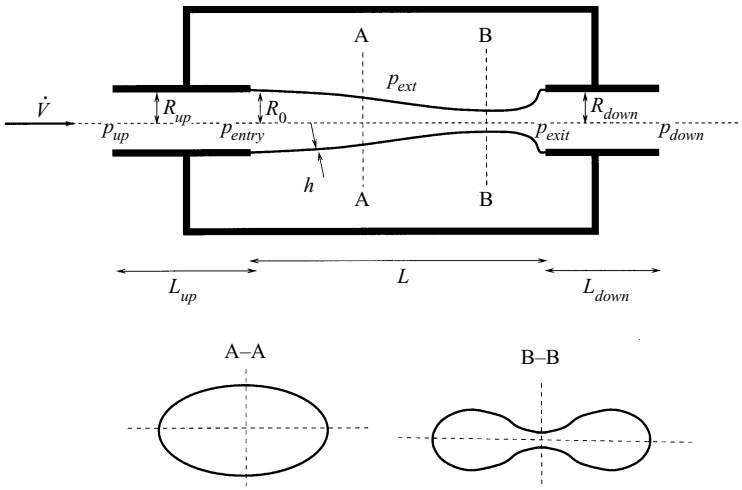


FIGURE 1. Sketch of a typical experimental setup.

The problem of flow in collapsible tubes has been studied experimentally by many authors (e.g. Conrad 1969; Gavriely *et al.* 1989; Bertram, Raymond & Pedley 1990, 1991; Elad *et al.* 1992) and the typical experimental setup shown in figure 1, forms the basis for most theoretical analyses: inside a pressure chamber, a thin elastic tube (typically made of rubber) of length L, undeformed radius R_0 and wall thickness h is mounted on two rigid tubes. The chamber pressure, p_{ext}, can be prescribed independently of the fluid pressure. Viscous fluid is pumped through the tube at a steady flow rate (volume flux $\dot{V}$). As in the physiological examples, the tube's non-axisymmetric collapse is often followed by large-amplitude self-excited oscillations.

The first theoretical investigations attempted to model the tube with simple lumped parameter models (e.g. Katz, Chen & Moreno 1969; Conrad 1969) which were able to reproduce some of the experimentally observed flow characteristics. However, they were unable to predict any details of the tube's deformation. One-dimensional models in which the flow was averaged over the tube's cross-section were developed next (see e.g. Shapiro 1977). In these models the tube's deformation was described by so-called 'tube laws' which are functional relationships between the tube's cross-sectional area and the local transmural pressure. Depending on the range of the Reynolds numbers considered, two distinct flow-limiting mechanisms can be found: wave-speed limitation in the high-Reynolds-number models and viscous flow limitation in the models concerned with lower-Reynolds-number flows (see e.g. Wilson, Rodarte & Butler 1986).

Various modifications to the one-dimensional equations were proposed to include the effects of flow separation (Cancelli & Pedley 1985), the wall's axial tension and its axial bending stiffness (Reyn 1987; McClurken *et al.* 1981). However, most of these modifications were introduced on an *ad hoc* basis.

In order to develop a more rational model of the problem while avoiding the complexities and computational requirements of a fully three-dimensional computation, several authors (Pedley 1992; Rast 1994; Lowe & Pedley 1995; Luo & Pedley 1995, 1996; Shin 1996) examined the two-dimensional equivalent of the collapsible tube problem: the zero (or finite) Reynolds number steady (or unsteady) flow in a two-dimensional channel in which part of one wall is replaced by an elastic membrane.

https://doi.org/10.1017/S0022112097007490 Published online by Cambridge University Press

These studies provided a detailed picture of the fluid and solid mechanics involved in the large-amplitude self-excited oscillations in this simplified system.

In another series of studies (Heil 1995, 1996; Heil & Pedley 1995, 1996), the steady deformations of the fully coupled three-dimensional system were investigated: the tube wall was modelled as a circular cylindrical shell and geometrically nonlinear shell theory was used to model its large non-axisymmetric post-buckling deformation. The fluid flow was modelled using lubrication theory (assuming low Reynolds numbers and a small wall slope in the direction of the flow). The results revealed many features which are unique to the three-dimensional geometry, such as snap-through buckling of the tube wall, flow division into the two lobes which remain open during the buckling, buckling with higher circumferential wavenumbers for increased upstream pressure, etc. This model provides a very accurate description of the tube's deformation but some of the assumptions used in the simplification of the fluid equations were violated (after the buckling, the wall slope at the downstream end tends to be quite large).

In order to develop the first entirely self-consistent model of the flow of viscous fluid in a collapsible tube, the small-slope assumption was abandoned and the lubrication theory was replaced by a solution of the steady three-dimensional Stokes equations which describe the flow in arbitrary geometries at zero Reynolds number. This paper presents the results of this study.

The paper is organized as follows: §2 gives a brief summary of the shell theory used to describe the wall deformation and presents the governing fluid equations. The numerical solution of the coupled problem is sketched briefly in §3. The computational results are presented in §4: first we give examples for typical wall deformations and the corresponding three-dimensional flow fields in the collapsed tube: then we present the flow characteristics of the tube (e.g. volume flux as a function of the applied pressure drop through the tube) for the four fundamental experimental setups and investigate the effect of variations in the tube's geometry. Section 5 describes an experiment in which the flow characteristics were measured and compared to the computational predictions. Finally, we discuss the implications that the results have for the above-mentioned modifications to the 'tube laws' used in previous investigations.

2. The model

2.1. *The shell equations*

We model a flexible tube of length L, undeformed midplane radius R_0 and wall thickness h as a cylindrical shell and describe its deformation using the geometrically nonlinear Kirchhoff–Love-type shell theory used in Heil & Pedley (1996). For a more detailed description of the shell theory see e.g. Wempner (1973). The deformation of the shell is expressed in terms of the dimensionless midplane displacements $\boldsymbol{v} = \boldsymbol{v}^*/R_0$. The superscript star distinguishes dimensional quantities from their non-dimensional equivalents. We use Lagrangian coordinates $\zeta^\alpha = \zeta^{*\alpha}/R_0$ (Greek and Latin indices have values 1, 2 and 1, 2, 3, respectively, and the summation convention is used) to parameterize the shell's midplane such that the non-dimensional vector to the undeformed midplane, $\boldsymbol{r}^0 = \boldsymbol{r}^{*0}/R_0$, is given by

$$\boldsymbol{r}^0 = \left(\sin(\zeta^2), \cos(\zeta^2), \zeta^1\right)^T, \quad \zeta^1 \in [0, L/R_0], \quad \zeta^2 \in [0, 2\pi]. \tag{1}$$

Then the position of a material point at a non-dimensional distance $\zeta^3 = \zeta^{*3}/R_0$ from the shell's undeformed midplane is given by

$$\boldsymbol{r} = \boldsymbol{r}^0 + \zeta^3 \boldsymbol{n}, \quad \zeta^3 \in [-h/(2R_0), h/(2R_0)], \tag{2}$$

https://doi.org/10.1017/S0022112097007490 Published online by Cambridge University Press

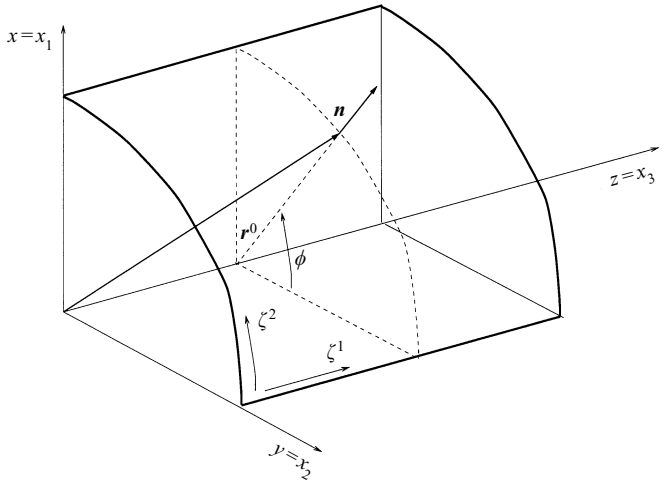


FIGURE 2. Sketch of the coordinate systems used in the analysis.

where $\boldsymbol{n} = \left(\sin(\zeta^2), \cos(\zeta^2), 0\right)^T$ is the vector normal to the undeformed midplane (see figure 2).

After the deformation, the material point on the midplane with the Lagrangian coordinates ζ^α has been displaced to a new position $\boldsymbol{R}^0(\zeta^\alpha) = \boldsymbol{r}^0(\zeta^\alpha) + \boldsymbol{v}(\zeta^\alpha)$. We decompose the displacement vector $\boldsymbol{v}$ into the undeformed basis, $\boldsymbol{v} = v^j \boldsymbol{a}_j$, where the undeformed base vectors are given by $\boldsymbol{a}_\alpha = \boldsymbol{r}^0_{,\alpha}$ and $\boldsymbol{a}_3 = \boldsymbol{n}$. The comma denotes the partial derivative with respect to the Lagrangian coordinates. Lowercase and uppercase letters are used for shell variables associated with the undeformed and deformed geometry, respectively.

The Kirchhoff–Love assumption states that material lines which were normal to the undeformed midplane remain normal to the shell's midplane throughout its deformation and that they remain unstretched. This assumption provides a good approximation for the shell's deformation, provided the ratio of wall thickness, h, to the minimum radius of curvature of the deformed shell remains small. With the Kirchhoff–Love assumption, the vector to an arbitrary material point in the shell after the deformation is given by

$$\boldsymbol{R} = \boldsymbol{R}^0 + \zeta^3 \, \boldsymbol{N}, \tag{3}$$

where $\boldsymbol{N}$ is the vector normal to the deformed shell.

In spite of the large deformations, the strain of the shell is typically fairly small which allows the use of Hooke's law as the constitutive equation (it should, however, be noted that many biological tubes are not well described by Hooke's law). Then the principle of virtual displacements, which governs the shell's deformation is given by (e.g. Wempner 1973)

$$\int_0^{2\pi} \int_0^{L/R_0} \left[E^{\alpha\beta\gamma\delta} \left(\gamma_{\alpha\beta} \, \delta\gamma_{\gamma\delta} + \frac{1}{12} \left(\frac{h}{R_0} \right)^2 \kappa_{\alpha\beta} \, \delta\kappa_{\gamma\delta} \right) - \left(\frac{R_0}{h} \right) (\boldsymbol{f} \cdot \delta\boldsymbol{R}) \, |_{\zeta^3 = \pm h/(2R_0)} \right] \mathrm{d}\zeta^1 \, \mathrm{d}\zeta^2 = 0, \tag{4}$$

where $\boldsymbol{f} = \boldsymbol{f}^*/E$ is the traction per unit area of the undeformed midplane, non-

https://doi.org/10.1017/S0022112097007490 Published online by Cambridge University Press

dimensionalized with Young's modulus E. $\gamma_{\alpha\beta}$ and $\kappa_{\alpha\beta}$ are the non-dimensional strain and bending tensors, respectively (given in the Appendix), and the dimensionless plane stress stiffness tensor, $E^{\alpha\beta\gamma\delta} = E^{*\alpha\beta\gamma\delta}/E$ is given by

$$E^{\alpha\beta\gamma\delta} = \frac{1}{2(1+\nu)}\left(\delta^{\alpha\gamma}\delta^{\beta\delta} + \delta^{\alpha\delta}\delta^{\beta\gamma} + \frac{2\nu}{1-\nu}\delta^{\alpha\beta}\delta^{\gamma\delta}\right), \tag{5}$$

where ν is Poisson's ratio.

The variations of strain and bending tensor have to be taken with respect to the displacements v^i and their derivatives. The tube is clamped at both ends. Therefore, at $\zeta^1 = 0$ and $\zeta^1 = L/R_0$ the displacements have to be prescribed and we have $\mathrm{d}v^3/\mathrm{d}\zeta^1 = 0$.

2.2. *The fluid equations*

2.2.1. *The Stokes equations*

For sufficiently low Reynolds number the Navier–Stokes equations, which govern the fluid flow, can be approximated by the linear Stokes equations given in dimensionless form by

$$\frac{\partial p}{\partial x_i} = \bar{\mu}\,\frac{\partial^2 u_i}{\partial x_j^2} \tag{6}$$

and the continuity equation

$$\frac{\partial u_i}{\partial x_i} = 0, \tag{7}$$

where

$$\bar{\mu} = \frac{\mu U}{R_0 E} \tag{8}$$

and μ is the dynamic viscosity of the fluid. In (6) and (7) the velocities were nondimensionalized with the average velocity through the tube, $u_i = u_i^*/U$, where $U = \dot{V}/(\pi R_0^2)$, and Young's modulus was used to non-dimensionalize the pressure, $p = p^*/E$. The Cartesian coordinates x_i^* were non-dimensionalized with the undeformed tube radius, $x_i = x_i^*/R_0$.

The Cartesian components of the fluid traction on the tube wall are given by

$$f_i = pN_i - \bar{\mu}\left(\frac{\partial u_i}{\partial x_j} + \frac{\partial u_j}{\partial x_i}\right)N_j, \tag{9}$$

where the N_i are the Cartesian components of the normal vector, $\boldsymbol{N}$, on the tube wall.

Suitable boundary conditions for the finite element discretization of these equations are the following. We prescribe a parabolic velocity profile at the far upstream end of the tube ($u_\alpha = 0,\ u_3 = 2\,[1-(x_1^2+x_2^2)/(1-(h/2R_0))^2]$) and require normal outflow at the downstream end ($u_\alpha = 0$). The weak form of the Stokes equations (which forms the basis of the finite element discretization) only allows us to prescribe the pressure at the tube's downstream end indirectly through a boundary condition for the normal component of the pseudo-traction. We set $-p + \bar{\mu}(\partial u_3/\partial x_3) = 0$ which sets the fluid pressure to zero since we have imposed parallel outflow.

2.2.2. *Lubrication theory*

During the early stages of the tube's collapse the wall slope in the axial direction, β say, is small. We can exploit this to simplify the fluid equations since the ratio of the typical radial and axial length scales is then given by β. Inserting this scaling into the

https://doi.org/10.1017/S0022112097007490 Published online by Cambridge University Press

continuity equation (7) shows that the ratio between the axial and transverse velocity components is also of that order, i.e. $u_3/u_\alpha = O(\beta)$. Then the momentum equations (6) show that at leading order the pressure is constant across each cross-section, i.e. $p = p(z)(1 + O(\beta))$. Therefore, the leading-order flow field is given by the simplified axial momentum equation

$$\frac{\partial p}{\partial z} = \bar{\mu}\left(\frac{\partial^2 u_3}{\partial x^2} + \frac{\partial^2 u_3}{\partial y^2}\right), \tag{10}$$

which is subject to the no-slip condition on the tube walls and to the normalization condition

$$\int_{A(z)} u_3 \, \mathrm{d}x \, \mathrm{d}y = \pi, \tag{11}$$

which ensures that the same volume flux passes through every cross-section. The equations are of parabolic character and if the volume flux is given, the pressure has to be prescribed at one axial coordinate, e.g.

$$p|_{z=0} = p_{entry}. \tag{12}$$

A fluid solver based on these equations was developed in Heil & Pedley (1996). We will assess the validity of the lubrication theory approximation in §§4.2 and 4.3.

2.2.3. *Flow through a slightly buckled tube*

In order to analyse the three-dimensional flow field in a slightly buckled tube we will now briefly consider the flow through a tube whose wall shape is given by $R(\phi, z) = 1 + \epsilon f(z)\cos(N\phi)$, where ϕ is the polar angle and $\epsilon \ll 1$. In order to approximate the shape of a slightly buckled tube, we choose $f(z)$ as

$$f(z) = \begin{cases} 0 & \text{for } z \in [-L_{up}, 0] \\ 14.3 \ \sin\left(\pi\left(1 - \dfrac{z}{L/R_0}\right)^2\left(\dfrac{z}{L/R_0}\right)^4\right) & \text{for } z \in [0, L] \\ 0 & \text{for } z \in [L, L + L_{down}]. \end{cases} \tag{13}$$

Since the wall's shape is prescribed, its elastic properties are irrelevant and we can set $\bar{\mu} = 1$. Hence we solve the Stokes equations in cylindrical polar coordinates, i.e.

$$\frac{\partial p}{\partial r} = \nabla^2 u_r - \frac{u_r}{r^2} - \frac{2}{r^2}\frac{\partial u_\phi}{\partial \phi}, \tag{14}$$

$$\frac{1}{r}\frac{\partial p}{\partial \phi} = \nabla^2 u_r - \frac{u_\phi}{r^2} + \frac{2}{r^2}\frac{\partial u_r}{\partial \phi}, \tag{15}$$

$$\frac{\partial p}{\partial z} = \nabla^2 u_z, \tag{16}$$

and the continuity equation

$$\frac{\partial u_r}{\partial r} + \frac{u_r}{r} + \frac{1}{r}\frac{\partial u_\phi}{\partial \phi} + \frac{\partial u_z}{\partial z} = 0. \tag{17}$$

The no-slip boundary conditions have to be applied on the buckled tube wall. We expand the velocity and pressure fields and the no-slip boundary condition with respect to the buckling amplitude ϵ, i.e. $\boldsymbol{u} = \boldsymbol{u}^{(0)} + \epsilon\boldsymbol{u}^{(1)} + ...$, $p = p^{(0)} + \epsilon p^{(1)} + ...$ and

$$\boldsymbol{u}|_{r=1+\epsilon f(z)\cos(N\phi)} = \boldsymbol{u}|_{r=1} + \epsilon f(z)\cos(N\phi)\left.\frac{\partial \boldsymbol{u}}{\partial r}\right|_{r=1} + ... = 0. \tag{18}$$

https://doi.org/10.1017/S0022112097007490 Published online by Cambridge University Press

The zeroth-order flow field is the Hagen–Poiseuille flow through the unbuckled tube, $\left[u_r^{(0)}, u_\phi^{(0)}, u_z^{(0)}, p^{(0)}\right] = \left[0, 0, 2(1-r^2), 8(\{L+L_{down}\}/R_0 - z)\right]$ and the boundary conditions for the perturbation velocities are

$$u_r^{(1)} = u_\phi^{(1)} = 0 \quad \text{at } r = 1 \tag{19}$$

and

$$u_z^{(1)} = -f(z)\cos(N\phi)\frac{\partial u_z^{(0)}}{\partial r} \quad \text{at } r = 1. \tag{20}$$

We expand the buckling mode $f(z)$ into an axial Fourier series,

$$f(z) = \sum_{k=-\infty}^{\infty} c_f^{(k)} \mathrm{e}^{\mathrm{i}\lambda_k z}, \tag{21}$$

where $\lambda_k = 2\pi/(L_{up} + L + L_{down})$. It can be shown that the general solution for the perturbation quantities has the form

$$\begin{pmatrix} u_r^{(1)} \\ u_\phi^{(1)} \\ u_z^{(1)} \\ p^{(1)} \end{pmatrix} = \sum_{k=-\infty}^{\infty} \sum_{j=1}^{\infty} \begin{pmatrix} c_r^{(jk)} \\ c_\phi^{(jk)} \\ c_z^{(jk)} \\ c_p^{(jk)} \end{pmatrix} \mathrm{e}^{\mathrm{i}\lambda_k z} \begin{pmatrix} r^{(N-1)+2(j-1)}\cos(N\phi) \\ r^{(N-1)+2(j-1)}\sin(N\phi) \\ r^{N+2(j-1)}\cos(N\phi) \\ r^{N+2(j-1)}\cos(N\phi) \end{pmatrix}. \tag{22}$$

We substitute these expansions into equations (14)–(17) and into the boundary conditions (19) and (20), separate the axial mode shapes and collect terms which are multiplied by equal powers of r. Upon truncating the double series after a finite number of terms, we obtain a system of linear equations from which the unknown coefficients $c_r^{(jk)}, c_\phi^{(jk)}, c_z^{(jk)}$ and $c_p^{(jk)}$ can be determined.

In the next section we will use this result to validate the numerical solution of the Stokes equations. The perturbation solution also shows two important features of the Stokes flow in a slightly buckled tube. First, at leading order the buckling does not change the overall pressure drop through the tube since the disturbance pressure, $p^{(1)}$, is periodic in the axial and circumferential directions (see also Lamb 1945, §332). Secondly, the boundary conditions (19) for the transverse perturbation are still homogenous. The transverse flow is driven by the axial wall slope, $\mathrm{d}f/\mathrm{d}z$, which enters the continuity equation (17) through the boundary condition (20) for the axial disturbance velocity.

3. The numerical solution

For the numerical solution of the coupled problem, the Stokes and shell equations were discretized with finite element methods. The coupled solution was then obtained by means of an iterative procedure based on the following scheme: start with an initial guess for the wall displacement field; solve the fluid equations in the corresponding tube geometry; determine the fluid traction and use it in the load terms in the shell equations; solve the shell equations for the tube's new equilibrium position and iterate until convergence.

Various modifications to this scheme had to be developed to make it robust enough to handle the strongly nonlinear behaviour of the coupled system and to achieve convergence within reasonable amounts of computer time. A displacement control technique was used to overcome the convergence problems associated with the shell's

https://doi.org/10.1017/S0022112097007490 Published online by Cambridge University Press

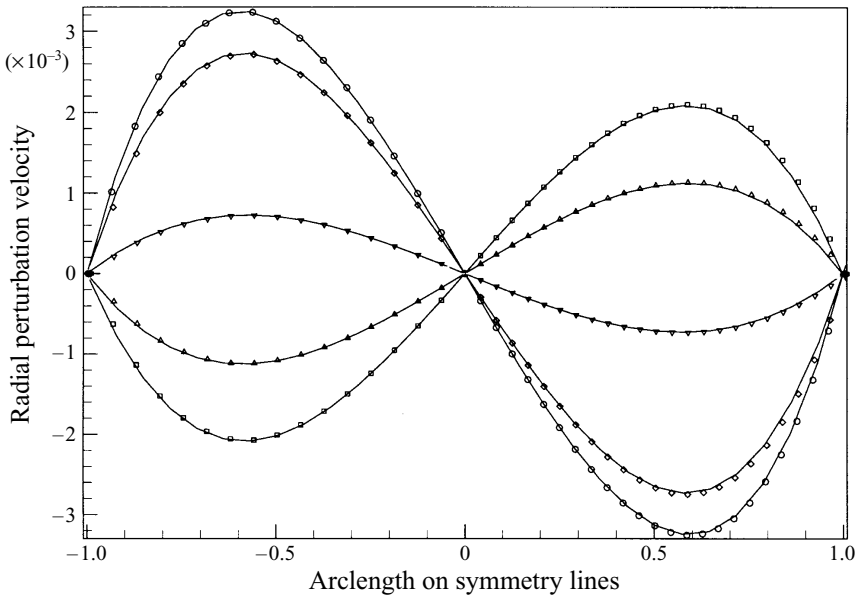


FIGURE 3. Comparison of the radial perturbation velocities for the flow in a slightly buckled tube ($\epsilon = 0.01$) as predicted by the perturbation analysis (solid lines) and the FEM computations (symbols). The quantities are plotted at five axial positions: $z = 5.0$ (□), $z = 6.0$ (△), $z = 7.0$ (▽), $z = 8.0$ (◇), $z = 9.0$ (○), along the two symmetry lines, $\phi = 0$ and $\phi = \pi/2$.

snap-through behaviour. An extrapolation procedure, based on the scheme's asymptotic convergence behaviour, was used to accelerate its convergence. An automatic mesh generator updated the fluid mesh as the tube wall deformed. The computations were carried out on the Cray C90 at the Pittsburgh Supercomputing Center. The code executed at approximately 300 MFlop/s and about 4–5 hours of CPU time were required to trace the tube's deformation over the whole range of deformations (from its initial axisymmetric shape to a strongly collapsed configuration). A more detailed description of the numerical technique is given in Heil (1997).

The shell solver was only modified slightly from the previous version which was documented in more detail in Heil & Pedley (1996). The newly developed Stokes solver was tested by using it to compute the flow through the undeformed tube (Hagen–Poiseuille flow). Furthermore, the predictions for the axial velocity component and the pressure distribution for the flow in a moderately buckled tube were compared to the results obtained from the lubrication theory solver, described in Heil & Pedley (1996). The agreement between the Stokes solver and the lubrication theory solver was very good as will be discussed in more detail in §4.2.

Finally, figure 3 shows the radial perturbation velocities at various axial positions in the slightly buckled tube considered in §2.2.3. The perturbation velocities are plotted along the two symmetry lines at $\phi = 0$ and $\phi = \pi/2$ (the arclength s along the symmetry lines is defined as: $s = -x_1$ on the vertical symmetry line and $s = x_2$ on the horizontal symmetry line). The symbols show the corresponding quantities obtained from the finite element solution and the agreement can be seen to be very good. The largest deviations occur near the boundaries since the perturbation solution does not fulfil the no-slip boundary condition on the real boundary; see (19).

https://doi.org/10.1017/S0022112097007490 Published online by Cambridge University Press

4. Computational results

In all computations, presented in the following sections, Poisson's ratio was set to $v = 0.49$ to reflect the near-incompressible behaviour of rubber tubes and biological tissues. In view of the relatively thick walled tubes (by the standards of thin shell theory) used in most experiments, the wall thickness was set to $h/R_0 = 1/20$ which is a value close to the upper limit of the applicability of thin shell theory. Unless otherwise stated, the tube's length was $L/R_0 = 10$ and two short rigid tubes upstream and downstream of the collapsible segment ($R_{up} = R_{down} = L_{up} = R_0,\ L_{down} = 2R_0$) were added to the computational domain (it was checked that doubling the length of the rigid tubes did not affect the results). To facilitate comparisons with previous work, the volume flux will be represented by the non-dimensional parameter

$$q = \frac{8\mu \dot{V} L}{\pi R_0^4 E} = 8\bar{\mu}\frac{L}{R_0}, \tag{1}$$

which can be identified as the non-dimensional pressure drop through the undeformed tube.

4.1. *The tube's deformation*

To illustrate the tube's behaviour we will first consider its deformation in a procedure in which the flow rate is prescribed by means of a volumetric pump attached to the tube's upstream end. We keep the fluid pressure at the tube's far downstream end constant, $p_{down} = 0$, and induce the tube's collapse by increasing the chamber pressure, p_{ext}.

For zero external pressure, $p_{ext} = 0$, the viscous pressure drop through the tube sets the entire flexible section under a positive transmural pressure. Hence the tube is inflated and it deforms axisymmetrically. Since the tube wall has a high extensional stiffness, its axisymmetric deformation is very small and the pressure drop through the tube is only slightly lower than the pressure drop in a rigid tube. As the chamber pressure is increased, the transmural pressure decreases and first becomes negative (compressive) at the tube's downstream end. When the compressive load exceeds a critical value, the axisymmetric deformation loses its stability and the tube buckles non-axisymmetrically. Figure 4 shows the tube's wall deformation as the non-axisymmetric collapse increases.

The tube's post-buckling deformation is governed by two competing effects. On the one hand, the tube's downstream end is always subject to the strongest compressive load and this tends to move the point of strongest collapse as far downstream as possible. On the other hand, the tube's high extensional stiffness favours deformations which minimize its axial extension. The axial extension is minimized for longitudinally symmetric buckling deformations for which the point of strongest collapse is near the centre of the tube.

For small amplitudes of the buckling deformation, the fluid pressure distribution differs only slightly from the pressure distribution in the undeformed tube, see §2.2.3. Hence, the compressive load on the tube wall increases approximately linearly with the distance from the upstream end. This asymmetry in the pressure distribution only induces a small asymmetry in the tube's deformation and the point of strongest collapse remains close to the tube's centre (figure 4*a, b*). As the buckling amplitude increases, the pressure drop in the most strongly collapsed part of the tube becomes more pronounced. The tube's downstream end becomes subject to a higher compressive load while the upstream end of the tube becomes inflated. The asymmetry of the

https://doi.org/10.1017/S0022112097007490 Published online by Cambridge University Press

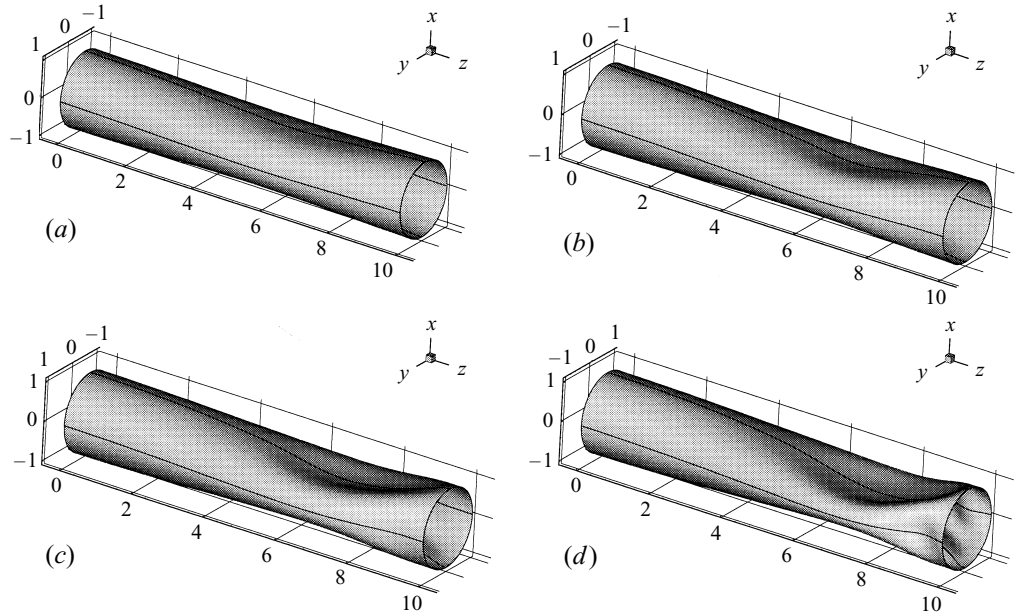


FIGURE 4. Tube deformation for constant volume flux ($q = 15.0 \times 10^{-5}$) and various values of the external pressure. $L/R_0 = 10$. (*a*) $p_{ext} = 1.96 \times 10^{-4}$, (*b*) $p_{ext} = 2.04 \times 10^{-4}$, (*c*) $p_{ext} = 2.68 \times 10^{-4}$, (*d*) $p_{ext} = 6.38 \times 10^{-4}$.

fluid traction increases with the tube's collapse, driving the point of strongest collapse more downstream. In the most strongly collapsed tube shown, the point of strongest collapse has moved to approximately 75% of the tube's length and the compressive transmural pressure near the tube's downstream end has become so large that two small regions on the tube's sidewalls have buckled inwards as well.

Figures 5(*a*) and 5(*b*) illustrate the effect of variations in the volume flux on the post-buckling deformation. In (*a*) a relatively small volume flux induces a moderate viscous pressure drop in the tube. The fluid pressure distribution only has a weak effect on the tube's deformation, which is dominated by the spatially constant external pressure. Hence, the tube's deformation is nearly symmetric in the axial direction. In (*b*), the tube's collapse is dominated by the strongly asymmetric fluid pressure, induced by a relatively high volume flux, and this leads to a strongly asymmetric deformation.

4.2. *The fluid flow*

Figure 6 shows the flow through four cross-sections in the most strongly collapsed part of the tube shown in figure 4(*d*). Due to the symmetry of the deformation only one quarter of each cross-section is shown. The contours indicate the magnitude of the axial velocity component. The tube's collapse increases the flow resistance in the strongly collapsed region near the tube's centreline. Consequently, the point of maximum axial velocity moves from the tube's centreline into the two side branches which will remain open when the opposite walls come into contact. The reduced cross-sectional area increases the peak axial velocity and the close proximity of the iso-velocity contours in the most strongly collapsed cross-section indicates a drastic increase in the axial wall shear stress.

https://doi.org/10.1017/S0022112097007490 Published online by Cambridge University Press

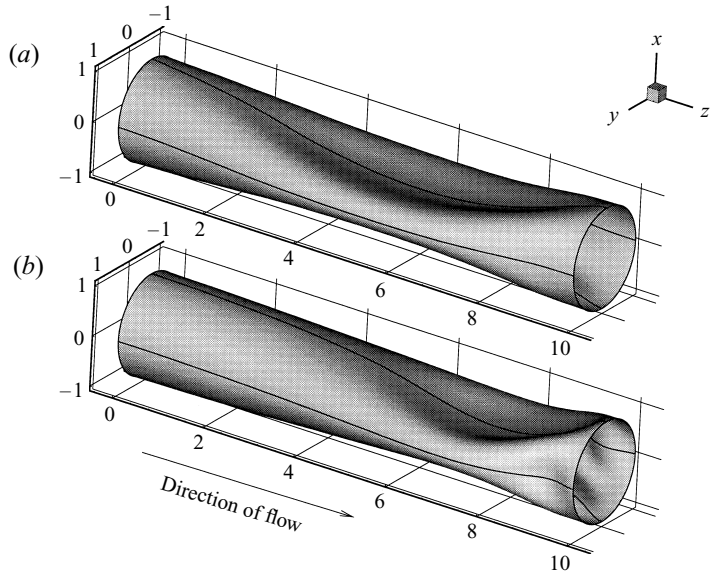


FIGURE 5. Two strongly collapsed tubes conveying different flow rates. (*a*) $q = 1.25 \times 10^{-5}$, $p_{ext} = 1.53 \times 10^{-4}$; (*b*) $q = 15.0 \times 10^{-5}$, $p_{ext} = 6.38 \times 10^{-4}$. $L/R_0 = 10$.

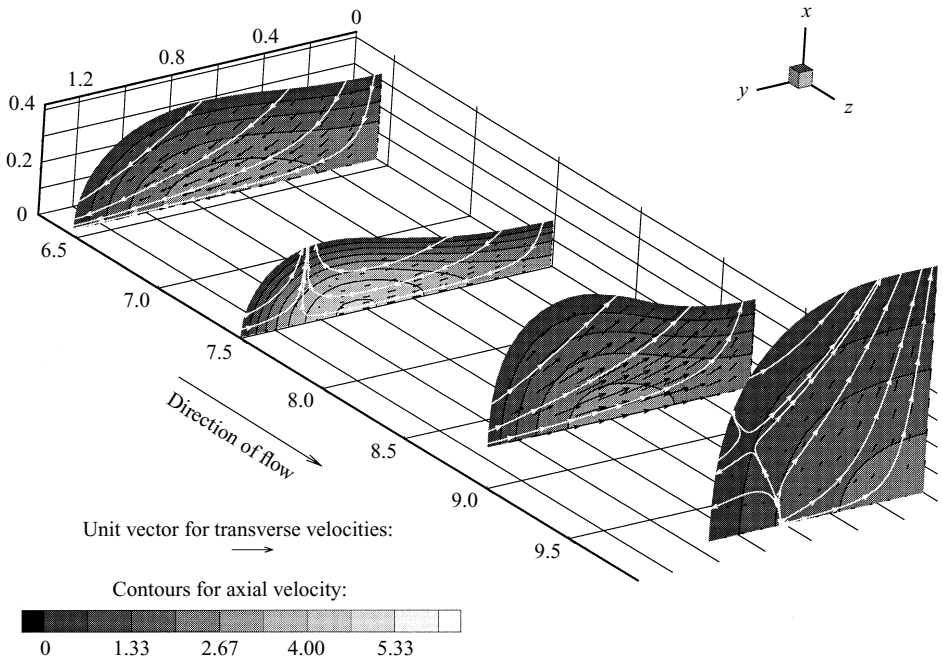


FIGURE 6. Flow through four cross-sections in the strongly collapsed tube shown in figure 4(*d*). Only one quarter of each cross-section is shown. The contours indicate the magnitude of the axial velocity, the black arrows show the transverse velocity components. The white lines are the transverse streamlines (in the x, y-plane). Cross-sections at $z = 6.43$, 7.49, 8.70 and 9.75. $L/R_0 = 10$, $q = 15.0 \times 10^{-5}$.

https://doi.org/10.1017/S0022112097007490 Published online by Cambridge University Press

The black arrows represent the magnitude and direction of the transverse velocity components. Upstream of the point of strongest collapse, the 'upper' part of the tube wall has a negative axial wall slope (it collapses more strongly towards the tube's centreline as one moves in the direction of the flow) whereas the 'sidewall' buckles increasingly outwards. The transverse flow follows this pattern and moves fluid from the 'upper' and central parts of the tube towards the 'sidewalls'. In the region where the tube re-opens, the transverse flow reverses its direction. Since the tube re-opens over a comparatively short axial length, the transverse flow in this region is stronger than in the upstream part. Near the point of strongest collapse (at $z \approx 7.5$), the transverse velocity components are very small. The transverse streamlines (shown in white) show that the transverse flow changes its direction gradually, thereby creating a stagnation point in the transverse flow field: near the 'sidewall', the flow has already changed its direction while the flow near the 'upper' wall is still the same as in the collapsing part of the tube. This is caused by a corresponding gradual change in the tube wall's axial wall slope: the 'sidewall' has already begun to move back towards the tube's centreline (as one moves in the direction of the flow) whereas the 'upper' wall is still collapsing inwards. This again shows the close relationship between the axial wall slope and the transverse flow field that was found in §2.2.3.

The final cross-section is located slightly downstream of the point of strongest collapse of the small buckled region on the tube's 'sidewall' (see figure 4*d*) and shows another interesting feature of the transverse flow field. The 'upper' part of the wall is unaffected by the formation of the small buckled region. Moving along the circumference in increasing y-direction, a region of positive wall slope is followed by a smaller region of negative wall slope as would be the case if the additional buckle were not present. In the lower part of the cross-section, the axial wall slope is positive again, reflecting the re-opening of the small buckled region. These wall slopes split the transverse flow field into two separate regions which feed into the two re-opening wall sections.

Figure 7 shows the fluid pressure distribution in the tube. The solid line represents the pressure on the tube's centreline. The broken lines show the pressure distribution along four different axial lines which follow the deforming fluid mesh. The pressure gradient in the slightly buckled upstream part of the tube is only slightly higher than in the rigid upstream tube. The flow resistance increases drastically in the most strongly collapsed part of the tube: the flow through the most strongly collapsed 20% of the tube's length accounts for about 80% of the total pressure drop. The difference between the pressures at various locations in the cross-section indicates the magnitude of the transverse pressure gradient which drives the transverse flow shown in figure 6. When the flow enters the downstream rigid tube, the transverse pressure gradient decays very quickly.

Figure 7 also shows the pressure distribution predicted by the lubrication theory approximation to the Stokes equations (solid line with symbols). Given that the wall slopes at the tube's downstream end are fairly large, lubrication theory provides a surprisingly good approximation to the real pressure distribution. Lubrication theory underestimates the overall pressure drop (by 3.6%) since it neglects the dissipation associated with the transverse flow components. The good agreement between lubrication theory and Stokes flow is closely related to fact that the overall pressure drop through the tube is dominated by the pressure drop in the most strongly collapsed region. In this region the wall slopes and transverse flow components are small and lubrication theory can be expected to provide a good approximation to the pressure distribution. The pressure drop in the regions with large wall slopes and large trans-

https://doi.org/10.1017/S0022112097007490 Published online by Cambridge University Press

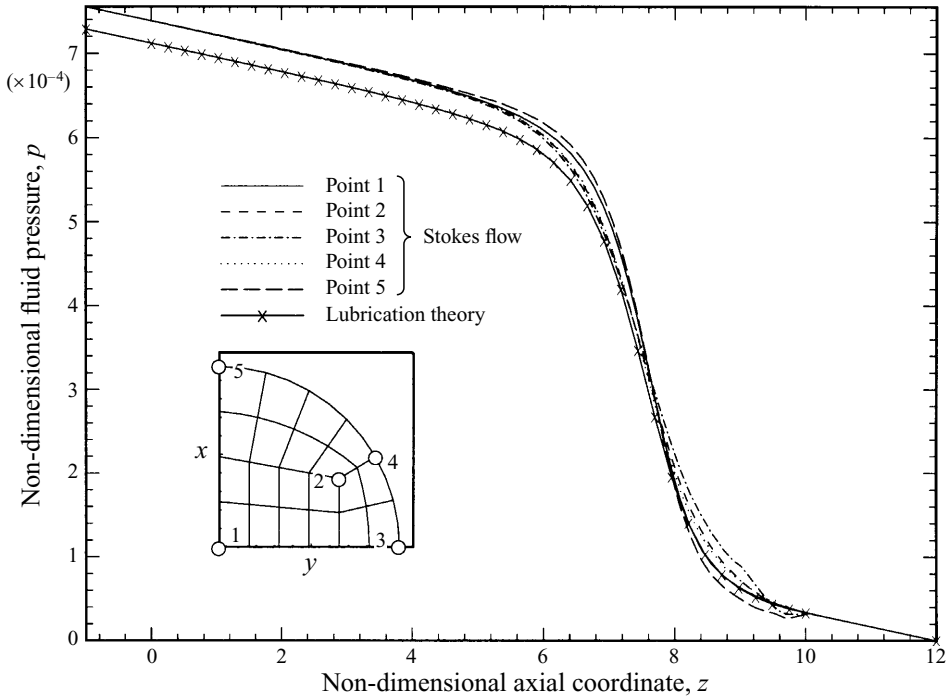


FIGURE 7. Pressure distribution through the strongly collapsed tube shown in figure 4(*d*). The pressure distribution along five different axial lines, whose position in the fluid mesh is indicated in the insert, is plotted as a function of the axial coordinate. The solid line with symbols shows the pressure distribution predicted by lubrication theory.

verse flow components is comparatively small, therefore the error introduced by the inappropriate use of lubrication theory in these regions is relatively insignificant.

4.3. *Flow characteristics*

Having analysed the wall deformation and the flow in the collapsed tube in some detail, we will now investigate the overall characteristics of the system. The observable parameters in an experiment are the volume flux, q, and three pressures: the upstream and downstream fluid pressures, p_{entry} and p_{exit}, and the chamber pressure p_{ext}. However, the tube's deformation is only affected by changes in the transmural pressures, therefore the system's state is completely determined by the specification of the volume flux and two pressure differences. Those can be chosen to be either the upstream and downstream transmural pressures, $p_{tm(up)} = p_{entry} - p_{ext}$ and $p_{tm(dn)} = p_{exit} - p_{ext}$, respectively, or one of these and the pressure drop through the tube, $\Delta p = p_{entry} - p_{exit}$. Depending on which parameter is kept constant and which one is used as the control parameter, different experimental procedures can be simulated.

Before analysing the data in terms of the characteristic pressure differences, we will first present the data in the form in which it was generated in the computations. In figure 8(*a*) the pressure drop through the tube is plotted as a function of the external pressure when the volume flux and the fluid pressure at the tube's far downstream end are held constant. Figure 8(*b*) shows the corresponding radial displacement of two material points on the tube wall (at $\zeta^1 = 7.4$ and $\zeta^2 = 0, \pi/2$) and thus gives an indication of the strength of the tube's collapse. For sufficiently low external pressure, the tube is inflated axisymmetrically and both radial displacements have the same

https://doi.org/10.1017/S0022112097007490 Published online by Cambridge University Press

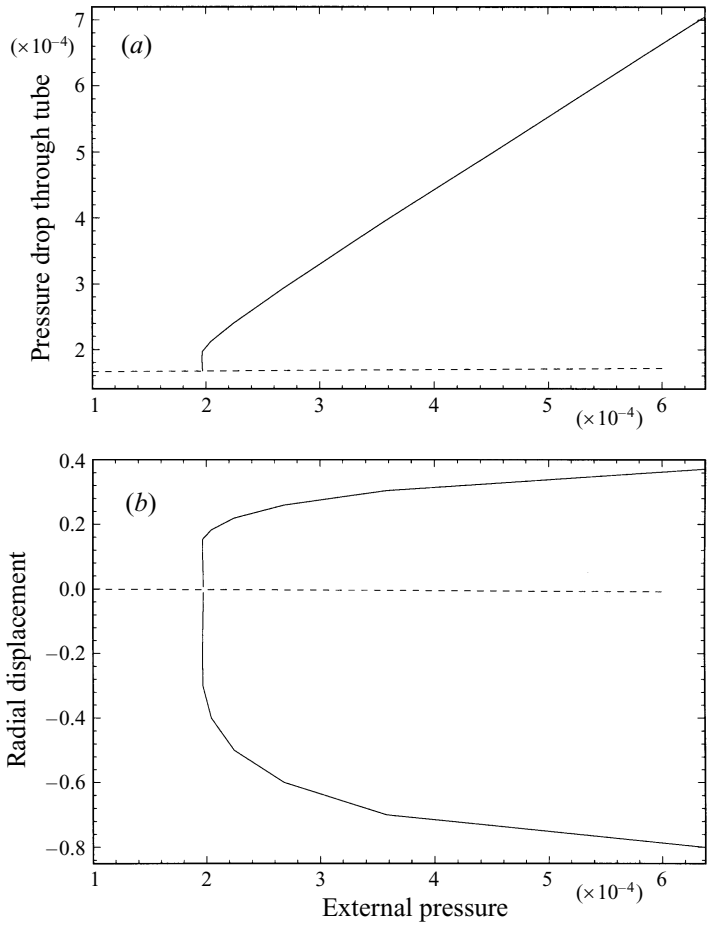


FIGURE 8. (*a*) Pressure drop through the tube ($\Delta p = p_{entry} - p_{exit}$) as a function of the external pressure, p_{ext}. (*b*) The corresponding tube deformation, characterized by the radial deformation of two material points (at $\zeta^1 = 7.4$ and $\zeta^2 = 0$ (upper solid line) and $\zeta^2 = \pi/2$ (lower solid line)). The volume flux and the far downstream pressure are held constant ($q = 15.0 \times 10^{-5}$ and $p_{down} = 0$). In both figures the dashed and solid lines represents the axisymmetric deformation and the post-buckling deformation, respectively. $L/R_0 = 10$.

value. Since the volume flux is held constant and the flow resistance changes little during the small axisymmetric pre-buckling deformation, the pressure drop through the tube changes very little with variations in the external pressure. The tube buckles when the external pressure exceeds a critical value: one material point collapses towards the tube's centreline (negative radial displacement), while the other one is pushed radially outwards (positive radial displacement). The diagram shows that the tube loses its stability via a subcritical bifurcation and buckles with a snap-through: the tube wall jumps into a significantly collapsed shape – one of the two material points is displaced by about 30% of the tube's radius. The corresponding point in figure 8(*a*) shows that this snap-through only induces a moderate jump in the pressure drop, Δp. As the external pressure is increased further, the tube's collapse is monotonic and the pressure drop rises approximately linearly with the external pressure.

A series of such computations was carried out with different values of the volume flux to map out the entire parameter space. We will now present the results of

https://doi.org/10.1017/S0022112097007490 Published online by Cambridge University Press

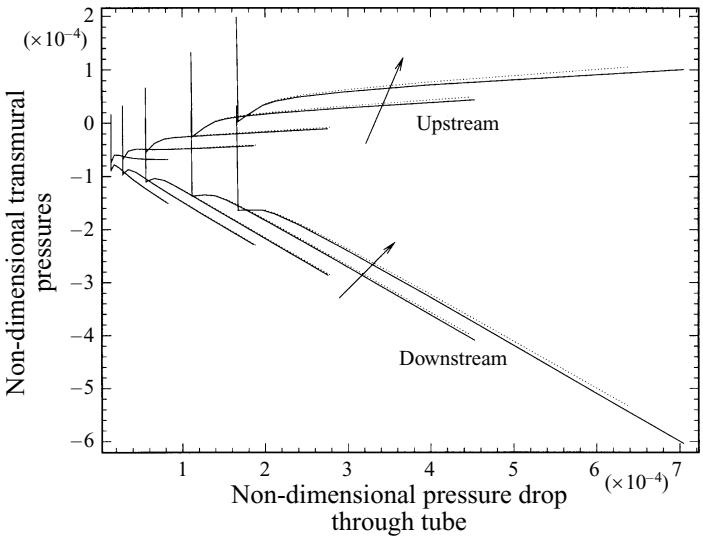


FIGURE 9. The flow characteristics obtained from the computations: upstream and downstream transmural pressures versus the pressure drop through the tube for constant flow rates. The solid lines are the curves obtained from the solution based on the Stokes equations. The dotted lines are the lubrication theory results. The arrows indicate the direction of increasing flow rate. $q = 1.25 \times 10^{-5},\ 2.5 \times 10^{-5},\ 5.0 \times 10^{-5},\ 10.0 \times 10^{-5}$ and 15.0×10^{-5}. $L/R_0 = 10$.

these studies in terms of the characteristic parameters q, $p_{tm(up)}$, $p_{tm(dn)}$ and Δp. The four parameter studies, discussed in the following subsections, correspond to the four fundamental experimental procedures in which one of the four characteristic parameters is held constant while another one is chosen as the control parameter.

4.3.1. $p_{tm}(\Delta p)$ *or* $\Delta p(p_{tm})$ *for* $q = const.$

Figure 9 re-displays the computational data in terms of the characteristic pressure differences. The upstream and downstream transmural pressures (upper and lower family of curves, respectively) are plotted as a function of the pressure drop through the tube while the volume flux, q, is held constant. The five pairs of curves correspond to five different values of the volume flux. The nearly vertical parts of the curves are the pre-buckling branches (on which an increase in the transmural pressures very slightly reduces the pressure drop through the tube). The pre-buckling pressure drop through the tube is proportional to the volume flux, therefore the curves corresponding to higher values of the volume flux are shifted to the right.

The tube buckles when the downstream transmural pressure becomes sufficiently negative. The snap-through behaviour shown in figure 8 manifests itself in the short region of increased downstream transmural pressure after the loss of stability. If the downstream transmural pressure is used as the control parameter then it remains constant during the tube's loss of stability. Therefore, the system jumps from the end of the pre-buckling curve to the intersection of the horizontal line $p_{tm(dn)} = \text{const.}$ with the post-buckling curve, thus causing a small jump in the pressure drop.

The diagram also shows that the snap-through behaviour disappears if one were to control the tube's collapse by increasing the pressure drop, Δp, while keeping the volume flux constant (the functions $p_{tm}(\Delta p)|_{q=const.}$ are single valued). This is, however, a rather theoretical prediction since it is not easy to envisage an experimental procedure which implements this control mechanism.

https://doi.org/10.1017/S0022112097007490 Published online by Cambridge University Press

The dotted lines in figure 9 are the approximate flow characteristics that are obtained when lubrication theory is used to compute the fluid traction. As one would expect, the agreement with the Stokes solution is very good for moderate tube collapse and the agreement remains surprisingly good in the large-displacement regime.

We will now investigate the flow characteristics for three different experimental setups. The flow characteristics shown in figures 10–12 below were generated by interpolating the computational data in the appropriate directions in parameter space. For this purpose a total of 37 runs with fixed q were carried out. Since lubrication theory provides a very good approximation of the flow characteristics, the interpolation was based on the data obtained from the lubrication theory solver which is computationally much cheaper.

4.3.2. *$q(\Delta p)$ or $\Delta p(q)$ for $p_{tm(up)} = const.$*

Figure 10 shows the volume flux through the tube as a function of the applied pressure drop. The transmural pressure at the upstream end of the collapsible tube is held constant along the curves. This situation could be realized experimentally by connecting the tube's upstream end to a large reservoir from which the fluid enters the collapsible segment at constant pressure. The flow would be driven by a volumetric pump, attached to the tube's downstream end, while the chamber pressure is held constant. For zero flow, the pressure drop through the tube vanishes and the entire tube is subject to a constant transmural pressure. For the curves shown, this pressure is higher (i.e. less compressive) than the tube's buckling pressure under a constant load. Therefore, the tube's deformation without throughflow is axisymmetric. As the pressure drop is increased (by decreasing the downstream transmural pressure) the flow rate increases approximately linearly while the downstream end of the tube becomes more strongly compressed. This part of the flow regime is described by the nearly straight line emanating from the origin. When the pressure drop and the compressive load on the downstream end reach a critical value, the tube buckles and the system undergoes a subcritical bifurcation. In figure 10, the critical parameter values $(\Delta p_{crit}, q_{crit})$ at which buckling occurs are determined by the intersection of the dotted post-buckling curves with the solid pre-buckling curve.

The critical pressure drop, Δp_{crit}, and volume flux, q_{crit}, rise with increasing upstream transmural pressure. This is because a larger viscous pressure drop is required to set the tube's downstream end under sufficiently strong compression to initiate the buckling when the upstream transmural pressure is raised.

The post-buckling behaviour depends strongly on which parameter (volume flux or pressure drop) is controlled and therefore held constant during the snap-through. First consider the case in which the pressure drop through the tube is controlled. In this case the value of the volume flux immediately after the snap-through is given by the intersection of the vertical line $\Delta p = \Delta p_{crit}$ with the post-buckling curve. The diagram shows that the large increase in the tube's flow resistance after the snap-through reduces the volume flux by a factor of about 2.

The behaviour after the snap-through depends on the magnitude of the upstream transmural pressure: for small values of $p_{tm(up)}$, a further rise in Δp increases the volume flux again. For larger values of $p_{tm(up)}$, a further increase in Δp diminishes the volume flux further as the increase in the flow resistance due to the increasing collapse outweighs the increase in the driving pressure drop. This behaviour is known as 'negative effort dependence' (see e.g. Kamm & Pedley 1989) and is observed during forced expiration. The system displays a pronounced hysteresis when the tube is re-opened by reducing the pressure drop. The tube jumps back into the axisymmetric

https://doi.org/10.1017/S0022112097007490 Published online by Cambridge University Press

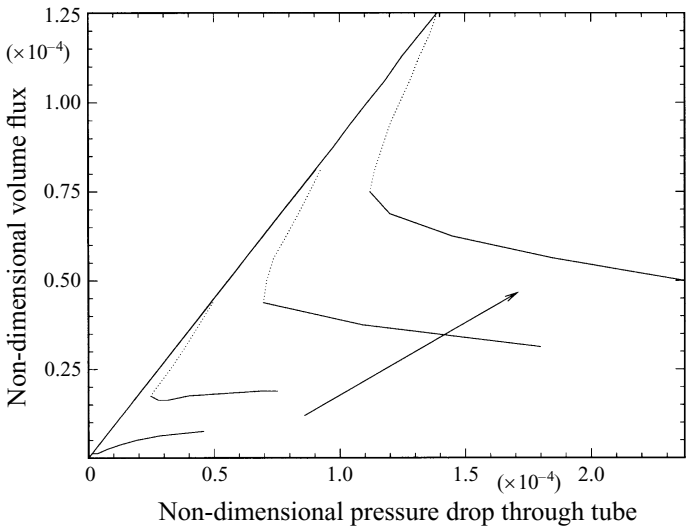


FIGURE 10. Flow characteristics (volume flux q as a function of the pressure drop through the tube, $\Delta p = p_{entry} - p_{exit}$) for constant upstream transmural pressure, $p_{tm(up)}$. The straight solid line represents the flow in the axisymmetric tube. The curved solid and dotted lines correspond to the stable and unstable parts of the post-buckling flow characteristics, respectively. The arrow indicates the direction of increasing upstream transmural pressure (note that increasing transmural pressure corresponds to a *decreasing* compressive load on the tube wall). $p_{tm(up)} = -1.15 \times 10^{-5}$, -3.43×10^{-5}, -5.70×10^{-5} and -7.98×10^{-5}. $L/R_0 = 10$.

shape when the ends of the stable post-buckling curves (solid lines) are reached. The pressure drop at which re-opening occurs is less than the value at which the tube collapses. The dotted part of the post-buckling curve is unstable and cannot be realized experimentally.

Let us now consider the second case in which the volume flux is controlled, as would be the case in the experimental setup envisaged at the beginning of this section. In this case the volume flux would remain constant during the tube's buckling and the pressure drop through the tube immediately after the snap-through would be determined by the intersection of the horizontal line $q = q_{crit}$ with the post-buckling curve. The diagram shows that no such intersection exists. All post-buckling curves in figure 10 end shortly before opposite wall contact occurs for the first time. Therefore, we conclude that the increase in the compressive load on the tube wall after the buckling is so large that it cannot be balanced by the restoring elastic forces. Under these conditions the entire length of the post-buckling curve is unstable. The tube buckles so strongly that its opposite walls come into contact. The opposite wall contact results in an overall stiffening of the tube which might be able to balance the strongly compressive fluid traction. Since the wall contact problem has not yet been incorporated into the model, we cannot investigate this region of parameter space. However, the results suggest the tube's loss of stability is followed by a strong collapse after which large areas of the wall would be in opposite wall contact (see also §5). In figure 9 this behaviour manifests itself as an increase in the upstream transmural pressure after the buckling.

4.3.3. *$q(\Delta p)$ or $\Delta p(q)$ for $p_{tm(dn)} = const.$*

Figure 11 shows the tube's flow characteristics for the case in which the downstream transmural pressure is held constant while the pressure drop and the volume flux

https://doi.org/10.1017/S0022112097007490 Published online by Cambridge University Press

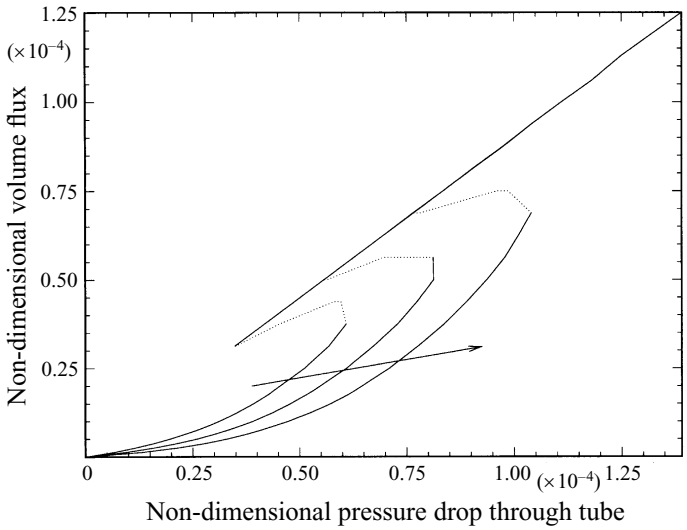


FIGURE 11. Flow characteristics (volume flux, q, as a function of the pressure drop through the tube, $\Delta p = p_{entry} - p_{exit}$) for constant downstream transmural pressure, $p_{tm(dn)}$. The straight solid line represents the flow in the axisymmetric tube. The curved solid and dotted lines correspond to the stable and unstable parts of the post-buckling flow characteristics, respectively. The arrow indicates the direction of decreasing downstream transmural pressure (note that decreasing transmural pressure corresponds to an *increasing* compressive load on the tube wall). $p_{tm(dn)} = -1.0 \times 10^{-4}, -1.1 \times 10^{-4}$ and -1.2×10^{-4}. $L/R_0 = 10$.

through the tube are varied. The corresponding experimental setup is similar to the one in the previous case, but the position of the reservoir and the volumetric pump have to be reversed. The values of the downstream transmural pressures for the three curves in figure 11 are lower (i.e. more compressive) than the tube's buckling pressure under a constant load. Without throughflow, the tube is therefore collapsed. As the pressure drop through the tube is increased (by increasing the upstream transmural pressure) the tube re-opens and thereby decreases its flow resistance. Therefore, the volume flux through the tube increases rapidly. Lowering the downstream transmural pressure increases the tube's collapse and leads to a larger pressure drop for a given volume flux. Therefore, the curves corresponding to lower values of $p_{tm(dn)}$ are shifted to the right. When the pressure drop reaches a critical value (at the ends of the solid lines) the tube wall jumps into an axisymmetric shape and re-opens completely. On the axisymmetric branch, the relation between flow rate and pressure drop is approximately linear. Again, we observe a strong hysteresis as we change from re-opening to collapsing.

If the volume flux is controlled (and therefore held constant during the snap-through buckling or re-opening), the displacement jump is accompanied by a sudden change in the pressure drop through the tube. The collapse is subcritical for either control parameter.

Figure 11 also shows that a reduction in the downstream transmural pressure increases the pressure drop at which the tube buckles. This can be explained as follows: a decrease in the downstream transmural pressure destabilizes the tube since it increases the compressive load on the tube's downstream end. A rise in the pressure drop increases the upstream transmural pressure and thus counteracts the destabilization by confining the compressed region to a smaller region near the tube's

https://doi.org/10.1017/S0022112097007490 Published online by Cambridge University Press

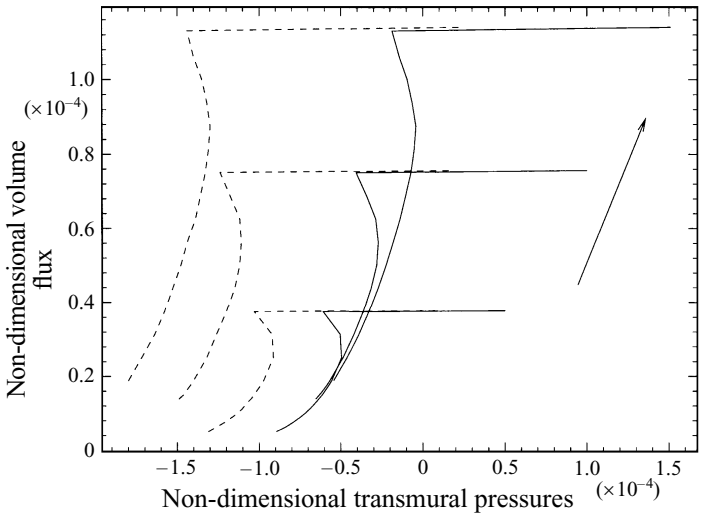


FIGURE 12. Flow characteristics (volume flux, q as a function of the transmural pressures) for constant pressure drop through the tube. Solid lines: upstream transmural pressure, $p_{tm(up)}$. Dashed lines: downstream transmural pressure, $p_{tm(dn)}$. The arrow indicates the direction of increasing pressure drop. $\Delta p = p_{entry} - p_{exit} = 0.42 \times 10^{-4}$, 0.84×10^{-4} and 1.26×10^{-4}. $L/R_0 = 10$.

downstream end. The inflated upstream part of the tube also exerts an axial tension on the compressed part and thus stabilizes it further.

4.3.4. *$q(p_{tm})$ or $p_{tm}(q)$ for $\Delta p = const.$*

Finally, we investigate the case in which the pressure drop through the tube is held constant (e.g. by connecting the upstream and downstream ends of the collapsible segment to large reservoirs at different heights). This case is representative for the flow of blood in the pulmonary capillaries, where the venous and arterial pressures are constant while the alveolar pressure is changed, e.g. during forced expiration. Figure 12 shows the volume flux through the tube as a function of the upstream and downstream transmural pressures (solid and dashed lines, respectively). The pressure drop is held constant along the curves and therefore determines the horizontal distance between the corresponding dashed and solid lines. When the upstream transmural pressure is larger than the pressure drop, the entire tube is inflated and the volume flux is nearly constant and proportional to the applied pressure drop. The tube collapses when the downstream transmural pressure becomes sufficiently negative. The loss of stability is again subcritical and the collapse reduces the volume flux by a factor of about 2. After the buckling a further reduction of the upstream (and downstream) transmural pressures increases the collapse further, monotonically reducing the volume flux.

If the volume flux were used as the control parameter (again, not an easy task experimentally since the pressure drop has to be kept constant along the curves), the loss of stability would be supercritical and the tube's collapse would increase continuously as the volume flux is decreased.

4.4. *Variations in the tube geometry*

All the results presented so far were obtained for one particular tube geometry. We will now investigate the effect of variations in the tube's length on its deformation and flow characteristics. Figure 13 shows a strongly collapsed tube which is twice as long ($L/R_0 = 20$) as that used in the above computations. As explained in §4.2, the viscous

https://doi.org/10.1017/S0022112097007490 Published online by Cambridge University Press

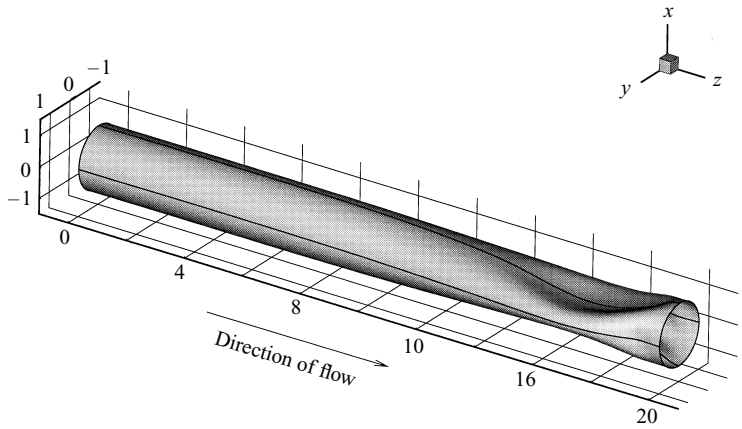


FIGURE 13. Strongly collapsed tube subject to $q = 10.0 \times 10^{-5}$, $p_{ext} = 2.88 \times 10^{-4}$. $L/R_0 = 20$.

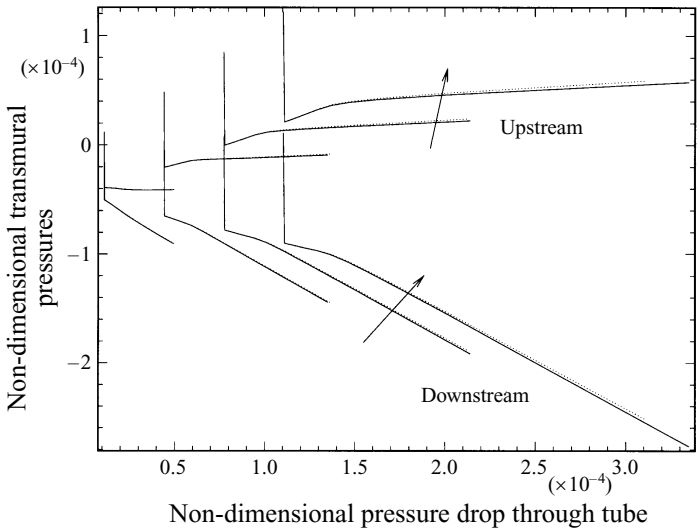


FIGURE 14. The flow characteristics obtained from the computations: upstream and downstream transmural pressures versus the pressure drop through the tube for constant flow rates. The solid lines are the curves obtained from the solution based on the Stokes equations. The dotted lines are the lubrication theory results. The arrows indicate the direction of increasing flow rate. $q = 1.0 \times 10^{-5},\ 4.0 \times 10^{-5},\ 7.0 \times 10^{-5}$ and 10.0×10^{-5}. $L/R_0 = 20$.

pressure drop moves the region of strongest collapse towards the tube's downstream end. Upstream of the collapsed region, the tube becomes inflated. Figure 13 shows that the same mechanism governs the deformation of longer tubes: an increase in the tube's length merely increases the length over which the tube is inflated. The deformation of the strongly collapsed region near the tube's downstream end remains virtually unaffected.

The tube's flow characteristics, shown in figure 14, are very similar to the ones obtained for the shorter tube. However, it should be noted that the increase in the tube's length changes the buckling behaviour under constant downstream transmural pressure and constant volume flux. The bifurcation changes from subcritical to supercritical and the snap-through behaviour disappears: the downstream transmural

https://doi.org/10.1017/S0022112097007490 Published online by Cambridge University Press

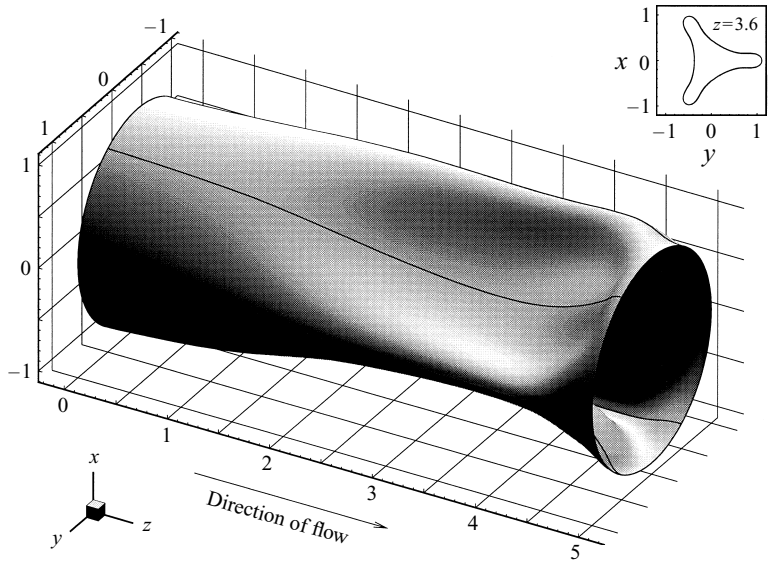


FIGURE 15. Strongly collapsed tube subject to $q = 45.0 \times 10^{-5}$, $p_{ext} = 3.31 \times 10^{-3}$. $L/R_0 = 5$. The tube buckles with three circumferential waves. The insert at the top right corner of the figure shows a cross-section through the tube at $z = 3.6$.

pressure decreases monotonically as the tube collapses. For sufficiently low volume flux, the same applies to the buckling under constant upstream pressure (e.g. the upstream transmural pressure for $q = 1.0 \times 10^{-5} = \text{const.}$ decreases monotonically as the tube collapses).

These effects are mainly due to the wall mechanics. An increase in the tube's length changes its buckling behaviour under a dead load (i.e. a load which does not change its magnitude as the tube deforms). Only tubes whose length to radius ratio, L/R_0, is less than a certain critical value (which depends on the tube's wall thickness, h/R_0, and its Poisson ratio, ν) buckle with a snap-through when subjected to a controlled external pressure.

If we control the transmural pressure at the tube's downstream end (where it is most compressive) we control the overall compression of the tube wall. Therefore, the buckling is similar to that under a controlled dead load and hence supercritical. Conversely, controlling the upstream transmural pressure does not control the compression of the tube's downstream end. For sufficiently high volume flux, the increase in the compressive load induced by the buckling is large enough to cause the strong collapse with immediate opposite wall contact if the upstream transmural pressure and the volume flux are held constant. Only if the volume flux is very small, such that the tube's post-buckling behaviour is dominated by the external pressure (as discussed in §4.1), does the increase in the tube's length change the buckling behaviour to a supercritical bifurcation.

A reduction in the tube's length has a more dramatic effect on its post-buckling deformation. It is well known from the stability analysis of cylindrical shells under external pressure (e.g. Yamaki 1984) that shorter cylindrical shells buckle with higher circumferential wavenumbers. The stability analysis of cylindrical shells conveying viscous flow (Heil 1996) confirmed this behaviour. The short tube shown in figure 15 ($L/R_0 = 5$) is strongly buckled in its most unstable buckling mode with $N = 3$

https://doi.org/10.1017/S0022112097007490 Published online by Cambridge University Press

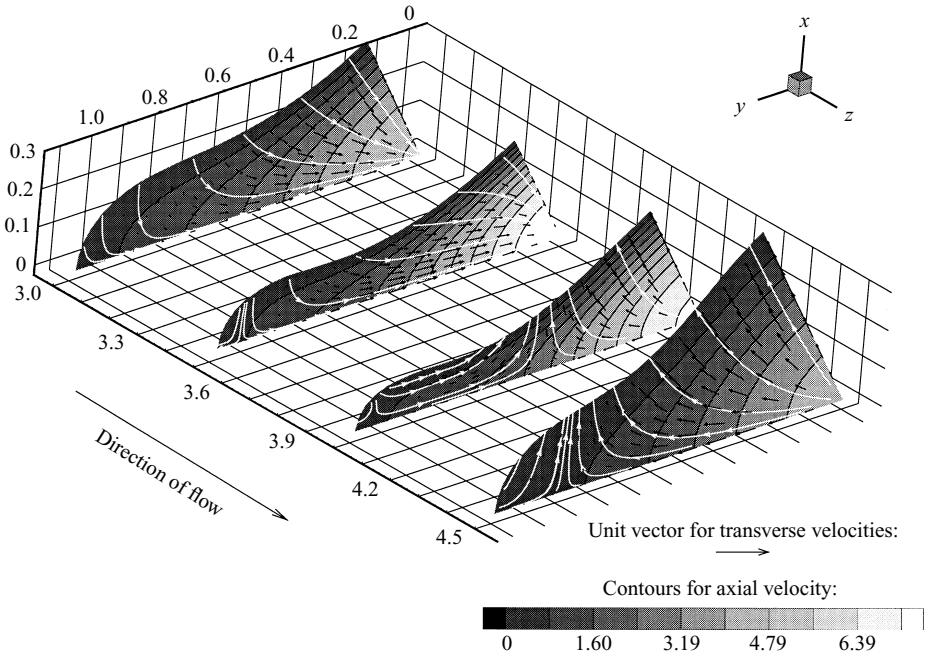


FIGURE 16. Flow through four cross-sections of the strongly collapsed tube shown in figure 15. Only one sixth of each cross-section is shown. The contours indicate the magnitude of the axial velocity, the black arrows show the transverse velocity components. The white lines are the transverse streamlines (in the x, y-plane). Cross-sections at $z = 3.0,\ 3.5,\ 4.0$ and 4.5. $L/R_0 = 5,\ q = 45.0 \times 10^{-5}$.

circumferential waves. A cross-section through the tube is shown in the insert at the top right corner of the figure. The flow through four cross-sections in the most strongly collapsed part of this tube is shown in figure 16. The contours for the axial velocity component show that a collapse in this buckling mode concentrates the flow near the tube's centreline where the flow resistance is lower than in the relatively narrow outer lobes. In the collapsing upstream part of the tube, the axial velocity increases in the streamwise direction and the transverse flow converges towards the tube's centreline. Again, the transverse streamlines reflect the variations in the tube's axial wall slope. During the early stages of the tube's collapse and in its weakly collapsed cross-sections, the radial displacement varies sinusoidally with the circumferential coordinate, i.e. $v^3 \sim \cos(N\zeta^2)$. Consequently, the collapsing sectors of the tube's wall alternate with sectors in which the wall bulges out. Since the tube has a high extensional stiffness, it always deforms such that its circumference remains approximately constant. For buckling patterns with two circumferential waves ($N = 2$), the bulging parts of the tube wall are therefore pushed further outwards as the tube collapses more strongly. An equivalent buckling pattern with a higher number of circumferential waves would lead to considerable circumferential stretching of the tube. Therefore, the collapsing parts of the wall pull the lobes, which were initially bulging out, towards the tube's centreline as the buckling amplitude increases. The corresponding changes in the axial wall slope result in the transverse flow patterns shown in figure 16.

It was shown in Heil (1996) and Heil & Pedley (1996) that longer tubes can also be forced to buckle with higher circumferential wavenumbers. For this purpose, one would have to subject the tube's upstream end to a large positive transmural pressure and increase the volume flux slowly. Due to the strong upstream pressurization, a

https://doi.org/10.1017/S0022112097007490 Published online by Cambridge University Press

substantial volume flux would then be required to compress the tube's downstream end. The tube buckles when a sufficient fraction of its length is subject to a sufficiently strong compression. For high upstream pressures, buckling occurs when a relatively small fraction of the tube's length is subject to a very high compressive load. Since the upstream part of the tube is still strongly inflated, it does not participate in the buckling and behaves like a rigid support for the short collapsing region. Hence the buckling in the collapsing part of the tube is very similar to the buckling of a shorter tube and the most unstable buckling wavenumber is increased.

The flow characteristics of the shorter tube ($L/R_0 = 5$) are qualitatively similar to those shown for the longer tube ($L/R_0 = 10$, see figure 9) but, due to the larger wall slopes in the shorter tube, the error introduced by the use of lubrication theory is slightly larger.

5. Experiments

It was pointed out in the introduction that the present study provides the first entirely self-consistent model of viscous flow in collapsible tubes. Therefore, we expect the computational results to be in good agreement with experimental observations. Virtually all previous experimental investigations of the flow in collapsible tubes were concerned with flows at significantly higher Reynolds numbers (a notable exception is Lyon, Scott & Wang's (1980) investigation into the applicability of the waterfall model for flow in collapsible tubes – the author is grateful to one of the referees for pointing out this reference). Therefore, a new experiment was designed and used to measure the flow characteristics of the collapsible tube. The experimental apparatus closely resembled the setup sketched in figure 1. A thin-walled rubber tube (wall thickness $h = 0.5$ mm, $E = 1.1 \times 10^6$ Pa, $\nu = 0.5$) was mounted on two Plexiglas tubes (inner radius $R_{up} = R_{down} = 3.15$ mm) whose ends had been machined to an outer radius very slightly larger than the undeformed radius of the collapsible tube ($R_0 = 4.2$ mm). Tightly fitting O-rings secured the collapsible tube onto the rigid tubes. Thick-walled rubber tubes connected the upstream rigid tube to a syringe pump which pumped high-viscosity silicon oil ($\mu = 9.0$ kg m^{-1} s^{-1}) through the system. At the downstream end, the oil drained into an open container. The pressure chamber was filled with water which made the oil-filled collapsible tube slightly buoyant ($\rho_{oil}/\rho_{water} \approx 0.97$). The chamber pressure, p_{ext}, was adjusted by varying the height of the water column in a transparent tube which was attached to the pressure chamber. Pressure transducers were attached to the rigid tubes to monitor the fluid pressures. The pressure taps were located $L_{up} = 15$ mm upstream and $L_{down} = 19$ mm downstream of the respective ends of the collapsible tube whose unsupported length was $L = 112$ mm. The collapsible tube was mounted with minimum axial pre-stretch and axial twisting.

The experiments were carried out at room temperature and the fluid viscosity was determined by measuring the pressure drop through a rigid reference tube. The changes in the pressure drop with variations in the volume flux confirmed Newtonian behaviour for the flow rates used in the experiments. The tube's elastic modulus was determined in uniaxial extension tests. These data varied considerably between measurements with different samples from the tube. The precise value of the elastic modulus used in the comparison with the computations was therefore obtained by matching the experimental and computational data for the flow through the undeformed tube.

The maximum Reynolds number, $Re = \bar{U} R_0 \rho_{oil}/\mu$, in the experiments was about 1.4×10^{-3}. The computations predict that a strong tube collapse increases the axial

https://doi.org/10.1017/S0022112097007490 Published online by Cambridge University Press

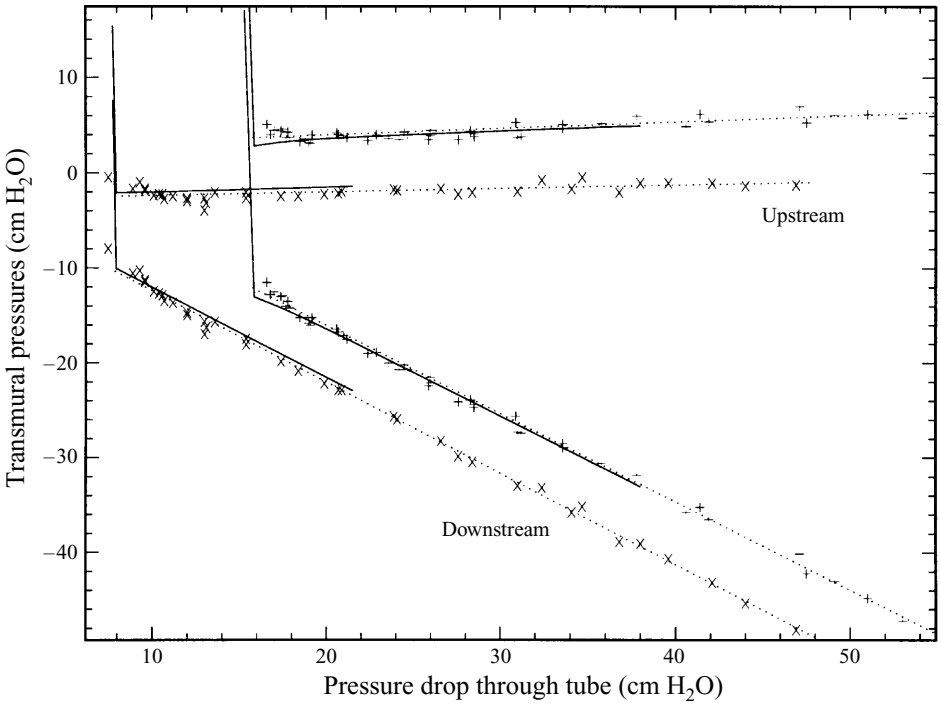


FIGURE 17. Comparison between computational predictions (solid lines) and experimental data (symbols) for the flow-characteristics of the collapsible tube used in the experiment. $\dot{V} = 5$ ml min^{-1} (+) and $\dot{V} = 2.5$ ml min^{-1} (×). $L/R_0 = 26.7$. The straight dotted lines were obtained by a least-squares fit to the experimental data points.

velocity by a factor of about 2–3. Therefore, we do not expect inertial effects to play a significant role in the experiments. It should be noted that the ratio $h/R_0 = 0.12$ in the experiments is somewhat too large properly to justify the use of thin-shell theory (see e.g. Wempner 1973).

In the experiments, the volume flux through the tube was held constant while the external pressure, p_{ext}, was varied to control the tube's collapse. The data were collected in several sweeps through the entire range of the tube's collapse, alternating between collapsing and re-opening.

Figure 17 shows the tube's flow characteristics (transmural pressures at the pressure taps, $p'_{tm(up)} = p_{up} - p_{ext}$ and $p'_{tm(dn)} = p_{down} - p_{ext}$, respectively, versus the total pressure drop, $\Delta p' = p_{up} - p_{down}$) for two different values of the volume flux. The solid lines are the computational results and the symbols represent the experimental data points. The straight dotted lines were obtained by a least-squares fit to the experimental data. They were plotted to show that the upstream transmural pressure does indeed have a slight tendency to increase as the tube collapses more strongly. This confirms the computational predictions of a strong collapse with immediate opposite wall contact if the tube's upstream pressure is held constant while the volume flux is increased to induce the tube's collapse (see §4.3.2).

The experimental data agree very well with the computational predictions. However, it should be noted that the experimental curves continue beyond the end of the computational curves which are restricted to tube shapes without opposite wall contact. Initially it had been hoped that the occurrence of opposite wall contact

https://doi.org/10.1017/S0022112097007490 Published online by Cambridge University Press

would affect the flow characteristics sufficiently to have a marked effect on these curves. Therefore, experimental data were collected up to a level of external pressure at which the appearance of a small flattened region in the most strongly collapsed part of the tube wall indicated that the opposite walls were effectively in contact (they were presumably still separated by a thin squeeze film. However, the flow resistance in the corresponding narrow gap between the walls would be so high that its presence would make little difference to the flow resistance of the entire cross-section). At precisely what value, $p_{ext}^{(c)}$, of the external pressure the opposite walls touched for the first time (in point contact) seemed impossible to assess with the present experimental setup. Figure 17 shows that the occurrence of opposite wall contact does not have a noticeable effect on the flow characteristics. The upstream (downstream) transmural pressures continue to increase (decrease) approximately linearly with the pressure drop through the tube. The decreasing downstream transmural pressure moves the point of strongest collapse further downstream while the tube's upstream end becomes more strongly inflated.

For even higher external pressures the tube's downstream end becomes so strongly collapsed that it is sucked into the downstream rigid tube. Ultimately, the experiment has to be terminated when the syringe pump fails to produce the required upstream pressures.

The experimental observation that the upstream transmural pressure continues to increase long after opposite wall contact has occurred for the first time casts some doubt on the existence of steady post-buckling deformations in the experimental setup discussed in §4.3.2 (controlled increase in the volume flux to induce the tube's collapse while keeping the upstream transmural pressure constant). It appears that the opposite wall contact is unable to stiffen the tube sufficiently to balance the strongly compressive fluid traction after the collapse. This would be in agreement with previous simple models of viscous flow limitations (e.g. Wilson *et al.* 1986).

Figure 18 shows a comparison between the computed and experimentally observed wall shapes. While no attempts were made to extract displacement data from the experiments, the visual agreement between computations and experiments can be seen to be quite good.

6. Discussion

The computational results and experimental observations presented here provide a detailed picture of the mechanisms governing the large-displacement fluid–structure interaction in this problem. However, in view of the computational cost associated with such detailed computations, it is desirable to investigate if the results obtained from this study can be used to improve simpler – ideally one-dimensional – models such that they capture the essential details of the system's behaviour.

Theories in which the flow is modelled one-dimensionally require a 'tube law' to establish a relation between the local transmural pressure and the tube's cross-sectional area. The main problem associated with a classical 'tube law' in which the transmural pressure is assumed to depend only on the local cross sectional area, $p(z) - p_{ext} = \mathscr{P}[A(z)]$, is that it does not allow the downstream boundary condition for the cross-sectional area to be satisfied. If the chamber pressure is constant then the viscous pressure drop reduces the transmural pressure in the direction of the flow. Consequently, the tube's cross-sectional area at the downstream end would have to be smaller than at the upstream end. This is not consistent with the boundary conditions for the wall deformation. In order to overcome this problem, various

https://doi.org/10.1017/S0022112097007490 Published online by Cambridge University Press

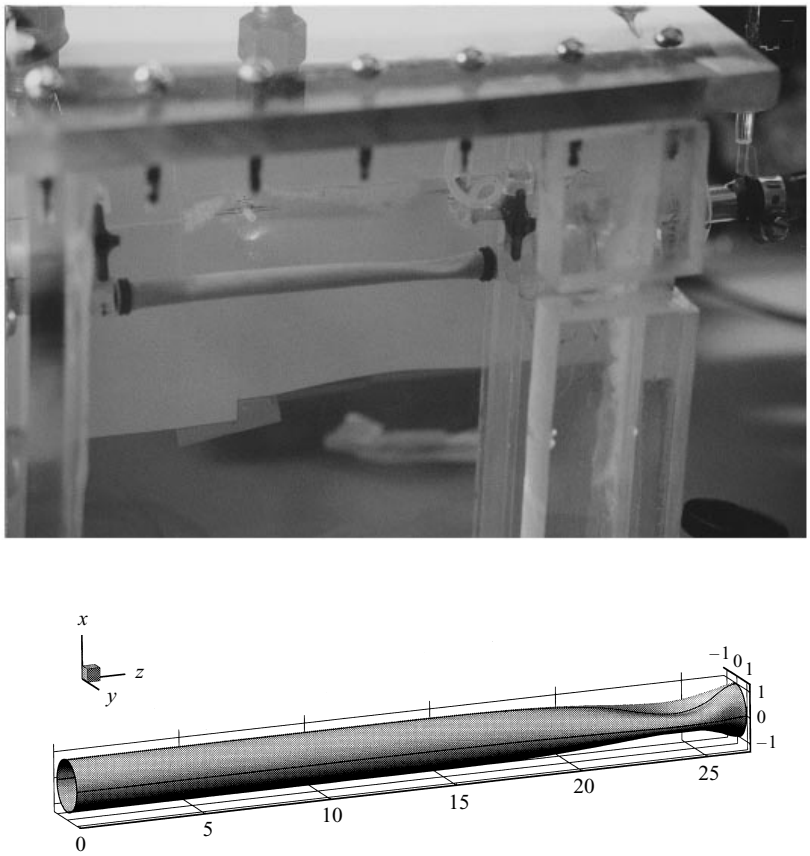


FIGURE 18. Comparison of the computed and experimentally observed wall shapes. $\dot{V} = 5$ ml min^{-1}, $p_{tm(down)} = -33$ cm H_2O, $L/R_0 = 26.7$.

authors (McClurken *et al.* 1981; Reyn 1987) modified the tube law by attempting to include the effects of longitudinal wall tension, T. They assumed that the cross-sections in the strongly collapsed parts of the tube are very flattened so that the flow through these cross-sections resembled the flow between two parallel membranes. Then the tube's cross-sectional area $A(z)$ is related to the axial wall curvature and the tube law can be written as

$$p(z) - p_{ext} = \mathscr{P}[A(z)] - T\frac{\partial^2 A}{\partial z^2}. \tag{24}$$

With this tube law, equal upstream and downstream cross-sectional areas are no longer equivalent to a vanishing pressure drop. The reduced downstream transmural pressure can be balanced by an increase in the axial wall curvature.

However, it has already been pointed out in Heil & Pedley (1996) that the tube shapes do not confirm the assumptions underlying the above modifications. The tube wall never appears flattened in a way that would make it behave like two parallel membranes. The moderately collapsed, nearly elliptical cross-sections of moderate aspect ratio are followed by dumbbell shaped cross-sections in which the flow is already splitting up into two separate side branches. Furthermore, it should be noted that the axial wall curvature has different signs in the collapsing and bulging sectors

https://doi.org/10.1017/S0022112097007490 Published online by Cambridge University Press

of the tube. Since the size of these sectors is comparable, it is not obvious if positive axial wall tension would tend to increase or decrease the average transmural pressure. It appears that the wall mechanics are inherently three-dimensional and that no simple decomposition into circumferential and axial contributions is possible.

It is, however, interesting to note that lubrication theory (which was shown to provide an excellent approximation to the fluid traction at zero Reynolds number) is in essence the fluid mechanics equivalent of the 'tube law'. It expresses the pressure gradient and shear stress as a function of the local shape of the tube's cross-section, very much in the same way as the solid mechanics 'tube law' expresses the cross-sectional area as a function of the local transmural pressure. While the coupling between lubrication theory and nonlinear shell theory is still significantly more complicated than a one-dimensional model, its numerical solution is an order of magnitude cheaper than the coupling with the full three-dimensional Stokes equations. It also manages to capture all the relevant mechanisms involved in the fluid–structure interaction.

While the present model enables us to investigate the system's behaviour at low Reynolds numbers it cannot be used to investigate the self-excited oscillations which are observed in many experiments since they tend to occur at higher Reynolds numbers. From a computational point of view, the coupled Stokes flow/shell theory solver, developed for this study, is a first step towards a simulation with finite Reynolds number and – ultimately – with time dependence.

The author wishes to thank Professor Roger Kamm, Dr Naomi Chesler and Dr Serhat Yesilyurt for many helpful discussions. Sara Godding helped carry out the experiment, the design of which was improved in many enjoyable discussions with Hayden Huang. The computations were carried out on the Cray C90 at the Pittsburgh Supercomputer Center. Financial support was provided by the German Academic Exchange Service through a NATO fellowship and by the EPSRC.

Appendix. The strain and bending tensors

The strain and bending tensors which describe the deformation of the shell in the variational principle (4) are obtained from the tangential base vectors to the deformed shell's midplane, $\boldsymbol{A}_\alpha = \boldsymbol{R}^0_{,\alpha}$. With the deformed midplane metric tensor $A_{\alpha\beta} = \boldsymbol{A}_\alpha \cdot \boldsymbol{A}_\beta$ the strain tensor is given by

$$\gamma_{\alpha\beta} = \tfrac{1}{2}(A_{\alpha\beta} - \delta_{\alpha\beta})$$

since the undeformed midplane metric is orthogonal (the undeformed midplane metric tensor is $a_{\alpha\beta} = \delta_{\alpha\beta}$). With the normal vector to the deformed shell, $\boldsymbol{N} = \boldsymbol{A}_1 \times \boldsymbol{A}_2/|\boldsymbol{A}_1 \times \boldsymbol{A}_2|$, the non-dimensional curvature tensor of the deformed midplane is $B_{\alpha\beta} = \boldsymbol{N} \cdot \boldsymbol{A}_{\alpha,\beta}$. The non-dimensional bending tensor is given by

$$\kappa_{\alpha\beta} = -(B_{\alpha\beta} - b_{\alpha\beta}),$$

where the only non-zero entry in the undeformed curvature tensor $b_{\alpha\beta}$ is $b_{22} = -1$.

Many authors derived approximate shell theories in which different approximations to these exact strain and bending tensors were used. However, it was shown in Heil & Pedley (1996) that the full nonlinear expressions have to be retained to obtain accurate results in the large-displacement regime.

https://doi.org/10.1017/S0022112097007490 Published online by Cambridge University Press

REFERENCES

Bertram, C. D., Raymond, C. J. & Pedley, T. J. 1990 Mapping of instabilities during flow through collapsed tubes of differing length. *J. Fluids Struct.* **4**, 125–153.

Bertram, C. D., Raymond, C. J. & Pedley, T. J. 1991 Application of nonlinear dynamics concepts to the analysis of self-excited oscillations of a collapsible tube conveying a flow. *J. Fluids Struct.* **5**, 391–426.

Cancelli, C. & Pedley, T. J. 1985 A separated flow model for collapsible tube oscillations. *J. Fluid Mech.* **157**, 375–404.

Conrad, W. A. 1969 Pressure-flow relationships in collapsible tubes. *IEEE Trans. Biomed. Engng* **BME-16**, 284–295.

Elad, D., Sahar, M., Avidor, J. M. & Einav, S. 1992 Steady flow through collapsible tubes: measurements of flow and geometry. *J. Biomech. Engng* **114**, 84–91.

Heil, M. 1995 Large deformations of cylindrical shells conveying viscous flow. PhD thesis, University of Leeds.

Heil, M. 1996 The stability of cylindrical shells conveying viscous flow. *J. Fluids Struct.* **10**, 173–196.

Heil, M. 1997 Stokes flow in an elastic tube – a large-displacement fluid-structure interaction problem. *Intl J. Numer. Meth. Fluids* (accepted).

Heil, M. & Pedley, T. J. 1995 Large axisymmetric deformations of a cylindrical shell conveying a viscous flow. *J. Fluids Struct.* **9**, 237–256.

Heil, M. & Pedley, T. J. 1996 Large post-buckling deformations of cylindrical shells conveying viscous flow. *J. Fluids Struct.* **10**, 565–599.

Gavriely, N., Shee, T. R., Cugell, D. W. & Grotberg, J .B. 1989 Flutter in flow-limited collapsible tubes: a mechanism for generation of wheezes. *J. Appl. Physiol.* **66**, 2251–2261.

Kamm, R. D. & Pedley, T. J. 1989 Flow in collapsible tubes: a brief review. *J. Biomech. Engng* **111**, 177–179.

Katz, A. I., Chen, Y. & Moreno, A. H. 1969 Flow through a collapsible tube. Experimental analysis and mathematical model. *Biophys. J.* **9**, 1261–1279.

Lamb, H. 1945 *Hydrodynamics.* Dover.

Lowe, T. W. & Pedley, T. J. 1995 Computation of Stokes flow in a channel with a collapsible segment. *J. Fluids Struct.* **9**, 885–905.

Luo, X. Y. & Pedley, T. J. 1995 Numerical simulation of steady flow in a 2-D collapsible channel. *J. Fluids Struct.* **9**, 149–197.

Luo, X. Y. & Pedley, T. J. 1996 A numerical simulation of unsteady flow in a 2-D collapsible channel. *J. Fluid Mech.* **314**, 191–225.

Lyon, C. K., Scott, J. B. & Wang, C. Y. 1980 Flow through collapsible tubes at low Reynolds numbers. Applicability of the waterfall model. *Circulation Res.* **47**, 68–73.

McClurken, M. E., Kececiogly, I., Kamm, R. D. & Shapiro, A. H. 1981 Steady, supercritical flow in collapsible tubes. Part 2. Theoretical studies. *J. Fluid Mech.* **109**, 391–415.

Pedley, T. J. 1992 Longitudinal tension variation in collapsible channels: a new mechanism for the breakdown of steady flow. *Trans. ASME: J. Biomech. Engng* **114**, 60–76.

Rast, M. P. 1994 Simultaneous solution of the Navier–Stokes and elastic membrane equations by a finite-element method. *Intl J. Numer. Meth. Fluids* **19**, 1115–1135.

Reyn, J. W. 1987 Multiple solutions and flow limitation for steady flow through a collapsed tube held open at the ends. *J. Fluid Mech.* **174**, 467–493.

Shapiro, A. H. 1977 Steady flow in collapsible tubes. *Trans. ASME: J. Biomech. Engng* **99**, 126–147.

Shin, J. J. 1996 The numerical simulation of flow through collapsible channels. PhD Thesis, MIT.

Wempner, G. 1973 *Mechanics of Solids.* McGraw-Hill.

Wilson, T. A., Rodarte, J. R. & Butler, J. P. 1986 Wave-speed and viscous flow limitation. In *Handbook of Physiology. Section 3: The Respiratory System*, Vol. III (ed. A. P. Fishman). American Physiological Society, Bethesda, Maryland.

Yamaki, N. 1984 *Elastic Stability of Circular Cylindrical Shells.* North-Holland.

https://doi.org/10.1017/S0022112097007490 Published online by Cambridge University Press